

Spin-layer locking induced second-order nonlinear effect in centrosymmetric crystals

Yanchong Zhao

Beijing National Laboratory for Condensed Matter Physics and Institute of Physics, Chinese Academy of Sciences <https://orcid.org/0000-0002-5472-8828>

Luojun Du

Aalto University <https://orcid.org/0000-0002-2420-8258>

Jing Liang

Academy for Advanced Interdisciplinary Studies, Peking University

Mohammad Bahramy

The University of Tokyo <https://orcid.org/0000-0001-9024-6335>

Mingwei Yang

Institute of Physics, Chinese Academy of Sciences

Yao Guang

Institute of Physics, Chinese Academy of Sciences, Beijing 100190, China University of Chinese Academy of Sciences, Beijing 100049, China <https://orcid.org/0000-0003-3238-8479>

Zheng Wei

Institute of Physics

Mengzhou Liao

Czech Technique university in Prague <https://orcid.org/0000-0003-0158-0548>

Jian Tang

Institute of Physics, The Chinese Academy of Sciences <https://orcid.org/0000-0003-1324-2466>

Jiaojiao Zhao

Institute of Physics

Cheng Shen

Institute of Physics, Chinese Academy of Sciences <https://orcid.org/0000-0001-7196-9239>

Xiaomei Li

Institute of Physics

Qinqin Wang

Beijing National Laboratory for Condensed Matter Physics and Institute of Physics, Chinese Academy of Sciences

Rong Yang

Beijing National Laboratory for Condensed Matter Physics and Institute of Physics, Chinese Academy of Sciences

Dongxia Shi

Beijing National Laboratory for Condensed Matter Physics and Institute of Physics, Chinese Academy of Sciences

Kaihui Liu

State Key Laboratory for Mesoscopic Physics, Frontiers Science Center for Nano-optoelectronics, School of Physics, Peking University, Beijing 100871 <https://orcid.org/0000-0002-8781-2495>

Zhipei Sun

Aalto University <https://orcid.org/0000-0002-9771-5293>

Guangyu Zhang (✉ gyzhang@iphy.ac.cn)

Institute of Physics, Chinese Academy of Sciences <https://orcid.org/0000-0002-1242-4391>

Article

Keywords: nonlinear principles, second-order nonlinear effect 29 (SONE)

Posted Date: December 29th, 2020

DOI: <https://doi.org/10.21203/rs.3.rs-126567/v1>

License: © ⓘ This work is licensed under a Creative Commons Attribution 4.0 International License.

[Read Full License](#)

Spin-layer locking induced second-order nonlinear effect in centrosymmetric crystals

Yanchong Zhao^{1,2}, Luojun Du^{3*}, Jing Liang^{4,5}, Mohammad Saeed Bahramy^{6,7}, Mingwei Yang^{1,2}, Yao Guang^{1,2}, Zheng Wei^{1,2}, Mengzhou Liao⁸, Jian Tang^{1,2}, Jiaojiao Zhao^{1,2}, Cheng Shen^{1,2}, Xiaomei Li^{1,2}, Qinqin Wang^{1,2}, Rong Yang^{1,9,10}, Dongxia Shi^{1,2,9}, Kaihui Liu^{4,5}, Zhipei Sun^{3,11} and Guangyu Zhang^{1,2,9,10*}

¹Beijing National Laboratory for Condensed Matter Physics; Key Laboratory for Nanoscale Physics and Devices, Institute of Physics, Chinese Academy of Sciences, Beijing, 100190, China

²School of Physical Sciences, University of Chinese Academy of Sciences, Beijing, 100190, China

³Department of Electronics and Nanoengineering, Aalto University, Tietotie 3, FI-02150, Finland

⁴State Key Laboratory for Mesoscopic Physics, Collaborative Innovation Center of Quantum Matter, Beijing, 100871 China

⁵School of Physics, Academy for Advanced Interdisciplinary Studies, Peking University, Beijing, 100871 China

⁶Quantum-Phase Electronics Center (QPEC) and Department of Applied Physics, The University of Tokyo, Tokyo 113-8656, Japan

⁷RIKEN Center for Emergent Matter Science (CEMS), Wako 351-0198, Japan

⁸Faculty of Electrical Engineering, Czech Technical University in Prague, Technicka 2, 16627 Prague 6, Czech Republic

⁹Beijing Key Laboratory for Nanomaterials and Nanodevices, Beijing 100190, China

¹⁰Songshan Lake Materials Laboratory, Dongguan, Guangdong, 523808, China

¹¹QTF Centre of Excellence, Department of Applied Physics, Aalto University, FI-00076 Aalto, Finland

*Corresponding author. Email: luojun.du@aalto.fi; gyzhang@iphy.ac.cn

Abstract

According to the generally accepted nonlinear principles, second-order nonlinear effect (SONE) is strongly inhibited by the crystalline symmetries and thus can manifest only in non-centrosymmetric materials with broken global spatial inversion symmetry. In stark contrast, here we report the observation of direct-current (DC) related SONE, including circular and linear photogalvanic effects, in centrosymmetric bilayer and multilayer MoS₂. In conjunction with relativistic first-principles calculations, we uncover that the observed DC-related SONE in inversion-symmetric MoS₂ results from the localized electronic states and the locking of spin with the layer and valley pseudospins. Our results provide a new insight into nonlinear physics and would be applicable to other phenomena thus far believed to occur only in non-centrosymmetric systems, such as quantum spin Hall effect, valley Hall effect, piezoelectricity and unconventional Ising superconductivity.

Introduction

Second-order nonlinear effect (SONE), such as circular/linear photogalvanic effect (CPGE/LPGE)¹⁻⁴, second-harmonic generation (SHG)⁵⁻⁸ and nonlinear Hall effect⁹⁻¹¹, breaks the limitations in linear response regime and sets a firm foundation for fascinating phenomena and technological advances. In the light of nonlinear principles^{12,13}, SONE under a driving electric field $\mathbf{E}(\omega)$ is described by the second-order nonlinear susceptibility pseudotensor $\eta_{abc}^{(2)}$:

$$\mathbf{S}_a(\text{DC}) = \eta_{abc}^{(2)}(\text{DC})\mathbf{E}_b(\omega)\mathbf{E}_c^*(\omega) \text{ or } \mathbf{S}_a(\text{AC}) = \eta_{abc}^{(2)}(\text{AC})\mathbf{E}_b(\omega)\mathbf{E}_c(\omega) \quad (1)$$

where $a, b, c \in \{x, y, z\}$ are the coordinate components, $\mathbf{S}(\text{DC})$ and $\mathbf{S}(\text{AC})$ are the responses of direct-current (DC) and alternating-current (AC) related SONE, respectively^{5,9,14-16}. Since both \mathbf{S} and $\mathbf{E}(\omega)$ are polar vectors and reverse the sign under the operation of inversion symmetry, SONE without higher-order photon wave vector effects is generally expected to vanish in centrosymmetric crystals with inversion symmetry of global crystal space group (see Supplementary Information)^{12,13}. However, being akin to recent studies of spatially localized spin polarization¹⁷⁻²⁵, Berry Curvature²⁶ and circular dichroism²⁷⁻³², one can imagine that for layered centrosymmetric crystal formed by two separated non-centrosymmetric constituent structural units, nonvanishing SONE can occur in each inversion-partner layer. Remarkably, if SONE from the two

separated inversion asymmetric units are the same, their superposition will produce a nonzero net response, making the observation possible.

Here we demonstrate experimentally the existence of DC-related SONE, including CPGE and LPGE, in centrosymmetric bilayer transition-metal dichalcogenide MoS₂, where inversion symmetry of global space group is present. Combining with electronic structure calculations with relativistic effects, we uncover that the observation of DC-related SONE in inversion symmetric bilayer MoS₂ can be understood as the locking of spin with the layer and valley degrees of freedom. Moreover, DC-related SONE responses increase monotonically with the number of layers. Such constructive nature of DC-related SONE photocurrents, together with the feasibility of doping control, provides a firm basis to enable advanced applications, such as compact, efficient and fast quantum photonics and photovoltaics.

Results and Discussion

Under optical excitation, the resulting nonequilibrium distribution of charge carriers in momentum space would cause the nonlinear photocurrent responses (e.g. CPGE and LPGE)¹³. Figure 1a depicts the schematic diagram for nonlinear photocurrent measurements as a function of rotation angle of quarter-wave plate (α). Unless otherwise specified, excitation is provided by a 633 nm (1.96 eV) laser radiation with an incidence (azimuthal) angle 35° (90°). The polarization-resolved photocurrents for an unbiased back-gate bilayer MoS₂ device on SiO₂ are presented in the upper panel of Figure 1c. In close analogy to the case of non-centrosymmetric monolayer MoS₂ (see Supplementary Information), polarization-dependent photocurrents of bilayer MoS₂ are comprised of four components and can be well described by the following phenomenological expression^{3,33,34}:

$$j_y(\alpha) = C \sin 2\alpha + L_1 \sin 4\alpha + L_2 \cos 4\alpha + D \quad (2)$$

The components of $C \sin 2\alpha$ accounts for the helicity-resolved photocurrent whose direction and magnitude depend on the chirality of light. The components of $L_1 \sin 4\alpha$ and $L_2 \cos 4\alpha$ correspond to the linear polarization-resolved photocurrents. The lower panel of Figure 1c shows the components of $C \sin 2\alpha$, $L_1 \sin 4\alpha$ and $L_2 \cos 4\alpha$ obtained by fitting. All these three polarization-dependent responses belong to DC-related SONE (see Supplementary Information)

and increase linearly with the laser power (Figure 1d). The last polarization-independent term D is photo-thermal current background.

To uncover the origin of $C \sin 2\alpha$, $L_1 \sin 4\alpha$ and $L_2 \cos 4\alpha$, we investigate the evolution of polarization-dependent photocurrents with laser spot positions. Figure 1d presents the results for a bilayer MoS₂ device with channel length of 2 μm . Note that the channel length is larger than the effective laser spot diameter (see Supplementary Information). The components of $C \sin 2\alpha$ and $L_1 \sin 4\alpha$ are largest when the laser spot is in the middle of channel, indicating intrinsic phenomena without contributions from contact. In contrast, the component of $L_2 \cos 4\alpha$ possesses the maximum when the laser spot is near contact, being akin to the photo-thermal current D , which has been well studied and origins from the laser-induced heat gradients^{3,14,35}. This indicates that the component of $L_2 \cos 4\alpha$ may harbor strong contribution from contacts and laser-induced heat gradients. Therefore, we do not focus on the component of $L_2 \cos 4\alpha$. Similar results can be found in monolayer MoS₂ device and bilayer MoS₂ devices with channel lengths of 3 μm and 4 μm (see Supplementary Information).

For helicity-resolved photocurrent $C \sin 2\alpha$, it can stem from two distinct physical mechanisms: CPGE or circular photon drag effect (CPDE). For CPGE, it belongs to a spin-polarized photocurrent and thus the direction is dependent on the spin state of photoexcited carriers. In other words, CPGE current will be reversed if the spin configuration of photogenerated carriers is changed. Figure 1f presents the helicity-resolved component of $C \sin 2\alpha$ measured under the same condition with two different laser energies: 633 nm (green) and 532 nm (red). Remarkably, the direction of photocurrent $C \sin 2\alpha$ reverses upon the variation of radiation energy. For a certain photon helicity, the photocurrent responses in bilayer MoS₂ under the excitations of 633 nm and 532 nm are dominated by A and B excitons with opposite spin configurations, respectively³⁶. Therefore, the change of sign for the direction of photocurrent $C \sin 2\alpha$ between 633 nm and 532 nm excitations indicates that component of $C \sin 2\alpha$ is dominated by CPGE, rather than CPDE which originates from the effect of retardation between electric field and instant velocity of charge carrier and is independent on the radiation frequency^{13,37,38}. Such assignment for the component of $C \sin 2\alpha$ is further confirmed by its evolution with incident angle Φ (see Supplementary Information). The absence of CPDE is

reasonable since it is determined by the derivative of $\eta_{abc}^{(2)}$ with respect to the photon wavevector \mathbf{q} (see Supplementary Information) and strongly suppressed at high frequency, e.g., the visible light used in our work¹³. For linear polarization-dependent photocurrent of $L_1 \sin 4\alpha$, it possesses the similar behavior with $C \sin 2\alpha$, such as laser position dependence (Figure 1e), change of sign upon the variation of laser frequency (Supplementary Figure 6) and incident angle Φ dependence (Supplementary Figure 5). This strongly indicates that their generation mechanisms are deeply related and $L_1 \sin 4\alpha$ should correspond to LPGE³.

Fairly surprisingly, our results unravel that DC-related SONE without photon wavevector effects (e.g., CPGE and LPGE) can present in bilayer MoS₂ where the global inversion symmetry of space group is restored as the lower layer is a π in-plane rotation of the upper layer (Figure 1b)^{27,28,39}. This goes against the generally accepted expectation that CPGE and LPFE are the exclusive territory of non-centrosymmetric materials with broken global inversion symmetry^{12,13}. Such anomalous phenomenon is confirmed in all our exfoliated bilayer samples (more than ten). Is this phenomenon an intrinsic property of inversion-symmetric bilayer MoS₂? To answer this question, it needs to rule out the interface effects since symmetry breaking can be possibly induced by the different dielectric environments between the upper and lower layers. We thus investigate the back-gate dependence of the polarization-resolved photocurrents with gate voltages from -80 V to 80 V (Figure 1g). If the DC-related SONE observed in bilayer MoS₂ is just an interface effect, it will fade to null at a certain gate voltage which can completely cancel the interface effect, akin to the recent valley Hall effect measurements²⁹. Interestingly, both CPGE and LPGE in bilayer MoS₂ can sustain over the whole gate range. This largely rules out the interface contributions and accordingly implies that the DC-related SONE is an inherent property of inversion symmetric bilayer MoS₂.

To further verify that centrosymmetric bilayer MoS₂ can indeed harbor nonzero DC-related SONE, we fabricated high quality, hexagonal boron nitride (*h*-BN) encapsulated and dual-gated bilayer MoS₂ devices by a dry transfer method (see Supplementary Information). Figure 2a shows the schematic diagram and optical microscope image of the dual-gate bilayer MoS₂ device. The corresponding atomic force microscopy (AFM) scanning is presented in Figure 2b. From the zoomed-in AFM image (inset of Figure 2b), it can be known that our sample displays a very low

root-mean-square surface roughness, i.e. 0.213 nm, indicating the ultraclean interface devoid of bubbles. Such encapsulated bilayer MoS₂ device with ultra-clean interface is superior to avoid the interface effects and unravel the intrinsic physical mechanism for DC-related SONE. Moreover, the dual gates allow us to continuously tune the out-of-plane displacement field \mathbf{D} over a wide range while maintaining the charge density n unchanged. The displacement field can modulate the global inversion symmetry of space group and is determined by $\mathbf{D} = (\epsilon_{rT}V_T/d_T - \epsilon_{rB}V_B/d_B)$, where $\epsilon_{rT}(\epsilon_{rB})$ and $d_T(d_B)$ are the relative dielectric constant and thickness of top (bottom) dielectric layer, respectively⁴⁰.

Figure 2c shows the back-gated transfer characteristics at different top gate voltages. Guided by the dual-gate tunability of electrical resistances, we are able to obtain diverse configurations with distinct \mathbf{D} while keeping n unchanged. The polarization-resolved photocurrents under different \mathbf{D} and constant n are presented in Figure 2d. Figure 2e shows the evolution of the CPGE (blue dots) and LPGE (green dots) photocurrents versus \mathbf{D} . It shows clearly that non-vanishing DC-related SONE with the same order of magnitude can be observed in dual-gate bilayer MoS₂ device over the whole range \mathbf{D} . The relatively small CPGE/LPGE photocurrent under negative \mathbf{D} may result from the contact resistance effect because contact resistance under negative \mathbf{D} is larger than that under positive \mathbf{D} (see Supplementary Information). To independently confirm that the global inversion symmetry of space group has been varied via \mathbf{D} and there is a global inversion-symmetry point at a certain \mathbf{D} , we performed SHG studies on the same device. Based on previous studies, SHG is a powerful and sensitive tool for probing the global inversion symmetry of space group. The integrated SHG intensity as a function of \mathbf{D} is presented in Figure 2e as red dots. The SHG intensity reaches the minimum at $\mathbf{D} = 0$ and increases squarely with \mathbf{D} . The SHG results rule out the symmetry breaking induced by external stimulus (e.g., electric field^{41,42} and current⁴³⁻⁴⁶) and unequivocally demonstrate that our bilayer MoS₂ at zero \mathbf{D} harbours the global inversion symmetry of crystal space group^{29,42}. Consequently, our results show undoubtedly that DC-related SONE can occur in centrosymmetric bilayer MoS₂ with inversion invariant global crystal space group.

To uncover the underlying physical origin of the observed DC-related SONE in inversion-symmetric bilayer MoS₂, we performed the relativistic first-principles calculations (see details in Methods). Figure 3a shows the orbital projected band structures of bilayer MoS₂. For

both the conduction and valance bands around K valley, the corresponding Bloch wavefunctions are predominantly from the d_{xy} , $d_{x^2-y^2}$ and d_{z^2} orbitals of Mo atoms that are confined within the 2D xy plane³⁹. Consequently, interlayer hopping energy between the Bloch wavefunctions of upper and lower layer is small, leading to localized electronic states. Together with giant spin-orbit coupling, the spin degrees of freedom is locked to layer pseudospin in a given valley, giving rise to hidden spin polarization^{17,20}. Figure 3b shows the calculated out-of-plane spin polarization of the doubly degenerate top valence band VB1 throughout the Brillouin zone, projected onto the upper and lower layers, respectively. The spin polarization is defined as $\rho = \frac{I(\uparrow) - I(\downarrow)}{I(\uparrow) + I(\downarrow)}$, where $I(\uparrow)$ and $I(\downarrow)$ denote the components of the spin-up and -down, respectively. For VB1 associated with A exciton and interested here, the out-of-plane spin polarization is segregated into different real-space domains and almost 100% (negative 100%) for K (-K) valley of upper layer and for -K (K) valley of lower layer. This indicates that for a given valley, the spin configuration is locked to the layer pseudospins, as shown in Figure 3c. In other words, the spin up (down) Bloch state is localized in upper (lower) layer in K valley, and vice versa in -K valley. Consequently, centrosymmetric bilayer MoS₂ can be regarded as two decoupled monolayers. Indeed, such decoupled nature in bilayer transition-metal dichalcogenides (TMDCs) has recently been confirmed by intrinsic circular dichroism²⁷⁻³⁰, unconventional Ising superconductivity⁴⁷⁻⁵⁰ and spin-orbitronics²⁰⁻²⁵.

Owing to the localized Bloch states and locking of spin with layer and valley pseudospins, the second-order susceptibility pseudotensor $\eta_{abc}^{(2)}$ of bilayer MoS₂ can be decomposed into two components stemmed from upper [$\eta_{abc}^{(2)}(u)$] and lower layers [$\eta_{abc}^{(2)}(l)$], respectively: $\eta_{abc}^{(2)} = \eta_{abc}^{(2)}(u) + \eta_{abc}^{(2)}(l)$. Since the inversion symmetry is explicitly broken in both upper and lower layers, $\eta_{abc}^{(2)}(u)$ and $\eta_{abc}^{(2)}(l)$ are non-vanishing. Due to the combination of threefold rotational symmetry of MoS₂ and DC nature of CPGE/LPGE, $\eta_{abc}^{(2)}(u)$ and $\eta_{abc}^{(2)}(l)$ should be the same in principle, leading to identical CPGE/LPGE photocurrent from upper and lower layers. To verify this view, we performed polarization-resolved photocurrent measurements for an unbiased monolayer MoS₂ device on SiO₂ under two configurations which are rotated by π with respect to each other (Figures 4a and 4c). Figures 4b and 4d show that CPGE/LPGE photocurrents keep invariant when we rotate the monolayer MoS₂ device 180° while keeping the incident light

unchanged. The invariance of CPGE/LPGE photocurrents for monolayer MoS₂ under the in-plane π rotation indicates that CPGE/LPGE photocurrents from its two constituent monolayers are the same in bilayer MoS₂. As a consequence, the CPGE/LPGE photocurrents in centrosymmetric bilayer MoS₂ are nonzero and the mere superposition of that in upper $J_{CPGE/LPGE}(u)$ and lower layers $J_{CPGE/LPGE}(l)$: $J_{CPGE/LPGE} = J_{CPGE/LPGE}(u) + J_{CPGE/LPGE}(l)$. Remarkably, due to the contributions from both upper and lower layer, CPGE/LPGE photocurrents in inversion-symmetric bilayer MoS₂ should be almost twice that in non-centrosymmetric monolayer case, in fair agreement with our measurements (see Supplementary Information).

We stress that above discussion on bilayer MoS₂ can be also applied to multilayer cases. Significantly, due to the increase of constituent monolayer units, the CPGE/LPGE photocurrents should increase with the number of layers. To rule out extrinsic factors, we choose an exfoliated MoS₂ sample with different number of layers (Figure 5a). Figure 5b presents the SHG mapping and single SHG spectra of distinct layers are shown in Figure 5c. The SHG intensity shows an even-odd oscillation with a decay envelope, in good harmony with the thickness dependent symmetry of global crystal space group⁵¹. The null SHG intensity for even layers (bilayer and quadrilayer) indicates the global inversion-symmetry of crystal space group. The layer dependences of polarization-resolved photocurrents are shown in Figure 5d. Figure 5e shows the CPGE component ($C \sin 2\alpha$) extracted by fitting. Intriguingly, CPGE spin photocurrent increases with thickness, which has been confirmed in other MoS₂ samples with thickness up to 136.6 nm (see Supplementary Information). Such constructive nature of CPGE spin photocurrents, together with the feasibility of doping control (Figure 1g), holds enormous promise to enable the manipulation of spin for exotic spintronics, ultrafast photonics and quantum-computation.

Finally, we point out that DC-related SONE provides a simple optical approach to detect the spin-layer locking effects in inversion-symmetric crystals. Compared to previous measurement methods, such as spin- and angle-resolved photoemission spectroscopy and circular polarization-resolved photoluminescence (PL) measurements, DC-related SONE shows some advantages. First, DC-related SONE can detect the spin-layer locking effects for a wide variety of centrosymmetric crystals, for example, semiconductor, semimetal and metal. In contrast, the helicity-resolved PL measurements can only be applied to a relative dearth of semiconductor with obvious PL response. Second, DC-related SONE can uncover the spin-layer locking effects for

materials ranging large-scale bulk to sub-micron-scale monolayer. While large bulk crystals are usually required for the high resolution in spin- and angle-resolved photoemission spectroscopy. Considering these, DC-related SONE will play a vital role in elucidating the spin-layer locking effects in the near future.

Conclusions

In conclusion, we demonstrate that DC-related SONE, including CPGE and LPGE, can occur in nonmagnetic centrosymmetric MoS₂. In conjunction with theoretical calculations, we uncover that the observed CPGE and LPGE in inversion-symmetric MoS₂ originate from the localized electronic states and valley dependent spin-layer locking effect. In addition, our results reveal that DC-related SONE responses increase monotonically with the number of layers and can be controlled by doping. The obtained results and knowledge in our work could largely expand the range of materials for nonlinear physics and provide a firm basis for the technological innovations in spintronics, communications, sensing and environmentally benign energy harvesting.

Methods

Device fabrications

All devices were fabricated by the standard micro-fabrication processes including e-beam lithography (EBL), metal evaporation and lifting-off. For back-gate devices, atomically thin flakes of MoS₂ were exfoliated from bulk MoS₂ crystals (2H phase) onto polydimethylsiloxane (PDMS) and then transferred onto SiO₂/Si substrates. The contact electrodes are Ti (2 nm)/Au (20 nm) as drain and source electrodes by e-beam evaporation. For dual-gate devices with ultra-clean interfaces, we first exfoliated *h*-BN on SiO₂ (300 nm)/Si (P++) substrate, then deposited source/drain electrodes (Ti (2 nm)/Au (7 nm)) onto it. As-made samples were thermal annealed in an Ar/H₂ atmosphere at 450°C then etched by moderate H₂ plasma etching to clean the residue or contaminations on the surface. Then we used Poly (Bisphenol A carbonate) (PC) supported by PDMS on glass slide to pick up *h*-BN and bilayer MoS₂ on the SiO₂ in sequence with accurate alignment based on an optical microscope. The number of layers for a MoS₂ sample was determined by optical contrast, Raman and PL spectra. Then we transferred *h*-BN/MoS₂ on the preformed electrode/*h*-BN substrate. Finally, few layers graphene was transferred on it as top gate

by dry transfer technique.

Photocurrent measurement setup

In our experiments, devices were wire-bonded onto a chip carrier and placed in a homemade optical chamber that combines electric transport measurements with laser illumination. All measurements, unless otherwise specified, were performed with 633 nm (1.96 eV) laser on-resonance with the A exciton of MoS₂ shining to devices in a configuration for an oblique incidence angle 35° and azimuthal angle 90°. Average laser power is 40 μW. The laser was focused on the channel of sample by a 50x (N.A.=0.5 W.D.=10.6 F.N.=26.5) or 10x (N.A.=0.25 W.D.=10.6 F.N.=22) Nikon objective. The chirality of laser is modulated by our electrical control quarter-wave plate which can rotate with a uniform speed, and we simultaneously detected the photocurrent by a semiconductor device analyzer (Agilent B1500A).

SHG measurements

In SHG experiments, the samples were excited by a femtosecond pulse laser centered at 820 nm with average power of 800 μW (Spectra-Physics Maitai laser, ~100 fs, 80 MHz). The linear polarized laser was normally incident and focus on samples by a Nikon objective (100x, N.A.=0.80). In reflection geometry, the generated SHG signal was directly collected by the same objective and recorded by a grating spectrograph (Princeton SP-2500i) with fixed integration time of 10 s. In the *D* dependent SHG experiments, the displacement field was applied through the dual gate independently controlled by two source meter units (Keithley 2400 Source-meter).

Relativistic first-principles calculations

The calculations were performed within density functional theory (DFT) using the modified Becke-Johnson exchange potential and Perdew-Burke-Ernzerh (PBE) of correlation functional as implemented in the WIEN2K program. Relativistic effects, including spin-orbit coupling, were fully included. The Brillouin zone was sampled by a 12x12x1 *k*-mesh. For the orbital and layer projection calculation, a tight binding Hamiltonian for the bulk band structure was constructed by downfolding the DFT results using maximally localized Wannier functions⁵²⁻⁵⁴, employing Mo 4d and 5s orbitals and S 3p and 3s orbitals as a basis.

Author contributions

G.Y.Z. supervised this work. Y.C.Z. and L.J.D. conceived of this project. Y.C.Z. fabricated the

devices, performed the photocurrent measurements with technical assistance from L.J.D. and M.W.Y. Y.C.Z. and L.J.D. performed data analysis. M.S.B. carried out *ab initio*-based tight-binding supercell calculations. J.L. performed the SHG measurements under the supervision of K.H.L. Y.C.Z., L.J.D., Z.P.S. and G.Y.Z. wrote the paper. All the other authors were involved in the discussion.

Acknowledgements

We would like to thank Feng Wang in UC Berkeley and Gui-Bin Liu in BIT for useful discussions, and Jimin Zhao, Xiufeng Han in IOP for technical support. G.Y.Z. thanks the National Science Foundation of China (NSFC) under the grant No.61888102 and 11834017, the Strategic Priority Research Program of Chinese Academy of Sciences (CAS) under the grant No. XDB0000000, the Key Research Program of Frontier Sciences of CAS under the grant No. QYZDB-SSW-SLH004, and the National Key R&D program under grant No. 2016YFA0300904. M.S.B gratefully acknowledges the financial support by CREST, JST (grant No. JPMJCR16F1).

Reference

- 1 Ganichev, S. D. & Prettl, W. Spin photocurrents in quantum wells. *J. Phys.: Condens. Matter* **15**, R935 (2003).
- 2 Xu, S. Y. *et al.* Electrically switchable Berry curvature dipole in the monolayer topological insulator WTe₂. *Nat. Phys.* **14**, 900-906 (2018).
- 3 McIver, J. W., Hsieh, D., Steinberg, H., Jarillo-Herrero, P. & Gedik, N. Control over topological insulator photocurrents with light polarization. *Nat. Nanotechnol.* **7**, 96-100 (2011).
- 4 Guan, H. M. *et al.* Photon wavelength dependent valley photocurrent in multilayer MoS₂. *Phys. Rev. B* **96**, 241304(R) (2017).
- 5 Autere, A. *et al.* Nonlinear Optics with 2D Layered Materials. *Adv. Mater.* **30**, e1705963 (2018).
- 6 Seyler, K. L. *et al.* Electrical control of second-harmonic generation in a WSe₂ monolayer transistor. *Nat. Nanotechnol.* **10**, 407-411 (2015).
- 7 Leo, N. *et al.* Magnetoelectric inversion of domain patterns. *Nature* **560**, 466 (2018).
- 8 Sun, Z. *et al.* Giant nonreciprocal second-harmonic generation from antiferromagnetic bilayer CrI₃. *Nature* **572**, 497-5013 (2019).
- 9 Sodemann, I. & Fu, L. Quantum Nonlinear Hall Effect Induced by Berry Curvature Dipole in Time-Reversal Invariant Materials. *Phys. Rev. Lett.* **115**, 216806 (2015).
- 10 Ma, Q. *et al.* Observation of the nonlinear Hall effect under time-reversal-symmetric conditions. *Nature* **565**, 337-342 (2019).

329 11 Kang, K., Li, T., Sohn, E., Shan, J. & Mak, K. F. Nonlinear anomalous Hall effect in
330 few-layer WTe₂. *Nat. Mater.* **18**, 324-328 (2019).

331 12 Shen, Y.-R. The principles of nonlinear optics. *New York, Wiley-Interscience, 1984, 575 p.*
332 (1984).

333 13 Glazov, M. M. & Ganichev, S. D. High frequency electric field induced nonlinear effects
334 in graphene. *Phys. Rep.* **535**, 101-138 (2014).

335 14 Ma, Q. *et al.* Direct optical detection of Weyl fermion chirality in a topological semimetal.
336 *Nat. Phys.* **13**, 842-847 (2017).

337 15 Sipe, J. E. & Shkrebtii, A. I. Second-order optical response in semiconductors. *Phys. Rev.*
338 *B* **61**, 5337-5352 (2000).

339 16 Quereda, J. *et al.* Symmetry regimes for circular photocurrents in monolayer MoSe₂. *Nat.*
340 *Commun.* **9**, 3346 (2018).

341 17 Zhang, X. W., Liu, Q. H., Luo, J. W., Freeman, A. J. & Zunger, A. Hidden spin
342 polarization in inversion-symmetric bulk crystals. *Nat. Phys.* **10**, 387-393 (2014).

343 18 Yuan, L. *et al.* Uncovering and tailoring hidden Rashba spin-orbit splitting in
344 centrosymmetric crystals. *Nat. Commun.* **10**, 906 (2019).

345 19 Wang, C. *et al.* Type-II Ising Superconductivity in Two-Dimensional Materials with
346 Spin-Orbit Coupling. *Phys. Rev. Lett.* **123**, 126402 (2019).

347 20 Riley, J. M. *et al.* Direct observation of spin-polarized bulk bands in an
348 inversion-symmetric semiconductor. *Nat. Phys.* **10**, 835-839 (2014).

349 21 Bertoni, R. *et al.* Generation and Evolution of Spin-, Valley-, and Layer-Polarized Excited
350 Carriers in Inversion-Symmetric WSe₂. *Phys. Rev. Lett.* **117**, 277201 (2016).

351 22 Razzoli, E. *et al.* Selective Probing of Hidden Spin-Polarized States in
352 Inversion-Symmetric Bulk MoS₂. *Phys. Rev. Lett.* **118**, 086402 (2017).

353 23 Guimaraes, M. H. D. & Koopmans, B. Spin Accumulation and Dynamics in
354 Inversion-Symmetric van der Waals Crystals. *Phys. Rev. Lett.* **120**, 266801 (2018).

355 24 Yao, W. *et al.* Direct observation of spin-layer locking by local Rashba effect in
356 monolayer semiconducting PtSe₂ film. *Nat. Commun.* **8**, 14216 (2017).

357 25 Tu, J. *et al.* Direct observation of hidden spin polarization in 2H- MoTe₂. *Phys. Rev. B*
358 **101**, 035102 (2020).

359 26 Cho, S. *et al.* Experimental Observation of Hidden Berry Curvature in
360 Inversion-Symmetric Bulk 2H- WSe₂. *Phys. Rev. Lett.* **121**, 186401 (2018).

361 27 Jones, A. M. *et al.* Spin-layer locking effects in optical orientation of exciton spin in
362 bilayer WSe₂. *Nat. Phys.* **10**, 130-134 (2014).

363 28 Zhu, B., Zeng, H., Dai, J., Gong, Z. & Cui, X. Anomalously robust valley polarization
364 and valley coherence in bilayer WS₂. *Proc. Natl. Acad. Sci. USA* **111**, 11606-11611
365 (2014).

366 29 Lee, J., Mak, K. F. & Shan, J. Electrical control of the valley Hall effect in bilayer MoS₂
367 transistors. *Nat. Nanotechnol.* **11**, 421-425 (2016).

368 30 Wu, S. F. *et al.* Electrical tuning of valley magnetic moment through symmetry control in
369 bilayer MoS₂. *Nat. Phys.* **9**, 149-153 (2013).

370 31 Liu, Q., Zhang, X. & Zunger, A. Intrinsic circular polarization in centrosymmetric stacks
371 of transition-metal dichalcogenide compounds. *Phys. Rev. Lett.* **114**, 087402 (2015).

372 32 Du, L. *et al.* Strongly distinct electrical response between circular and valley polarization

in bilayer transition metal dichalcogenides. *Phys. Rev. B* **99**, 195415 (2019).

33 Eginligil, M. *et al.* Dichroic spin–valley photocurrent in monolayer molybdenum disulphide. *Nat. Commun.* **6**, 7636 (2015).

34 Pan, Y. *et al.* Helicity dependent photocurrent in electrically gated $(\text{Bi}_{1-x}\text{Sb}_x)_2\text{Te}_3$ thin films. *Nat. Commun.* **8**, 1-9 (2017).

35 Zhang, Y. *et al.* Enhanced intrinsic photovoltaic effect in tungsten disulfide nanotubes. *Nature* **570**, 349-353 (2019).

36 Du, L. *et al.* Robust spin-valley polarization in commensurate MoS_2 /graphene heterostructures. *Phys. Rev. B* **97**, 115445 (2018).

37 Karch, J. *et al.* Dynamic Hall effect driven by circularly polarized light in a graphene layer. *Phys. Rev. Lett.* **105**, 227402 (2010).

38 Jiang, C. *et al.* Helicity-dependent photocurrents in graphene layers excited by midinfrared radiation of a CO_2 laser. *Phys. Rev. B* **84**, 125429 (2011).

39 Du, L. J. *et al.* Temperature-driven evolution of critical points, interlayer coupling, and layer polarization in bilayer MoS_2 . *Phys. Rev. B* **97**, 165410 (2018).

40 Taychatanapat, T. & Jarillo-Herrero, P. Electronic transport in dual-gated bilayer graphene at large displacement fields. *Phys. Rev. Lett.* **105**, 166601 (2010).

41 Lee, C., Chang, R. & Bloembergen, N. Nonlinear electroreflectance in silicon and silver. *Phys. Rev. Lett.* **18**, 167 (1967).

42 Klein, J. *et al.* Electric-field switchable second-harmonic generation in bilayer MoS_2 by inversion symmetry breaking. *Nano Lett.* **17**, 392-398 (2017).

43 Khurgin, J. B. Current induced second harmonic generation in semiconductors. *Appl. Phys. Lett.* **67**, 1113-1115 (1995).

44 Ruzicka, B. A. *et al.* Second-harmonic generation induced by electric currents in GaAs. *Phys. Rev. Lett.* **108**, 077403 (2012).

45 Wang, J., Zhu, B.-F. & Liu, R.-B. Second-order nonlinear optical effects of spin currents. *Phys. Rev. Lett.* **104**, 256601 (2010).

46 Werake, L. K. & Zhao, H. Observation of second-harmonic generation induced by pure spin currents. *Nat. Phys.* **6**, 875-878 (2010).

47 Xi, X. X. *et al.* Ising pairing in superconducting NbSe_2 atomic layers. *Nat. Phys.* **12**, 139-143 (2016).

48 Sohn, E. *et al.* An unusual continuous paramagnetic-limited superconducting phase transition in 2D NbSe_2 . *Nat. Mater.* **17**, 504-508 (2018).

49 Saito, Y. *et al.* Superconductivity protected by spin–valley locking in ion-gated MoS_2 . *Nat. Phys.* **12**, 144-149 (2015).

50 Cui, J. *et al.* Transport evidence of asymmetric spin–orbit coupling in few-layer superconducting 1Td- MoTe_2 . *Nat. Commun.* **10**, 1-8 (2019).

51 Li, Y. *et al.* Probing symmetry properties of few-layer MoS_2 and h-BN by optical second-harmonic generation. *Nano Lett.* **13**, 3329-3333 (2013).

52 Souza, I., Marzari, N. & Vanderbilt, D. Maximally localized Wannier functions for entangled energy bands. *Phys. Rev. B* **65**, 035109 (2001).

53 Mostofi, A. A. *et al.* wannier90: A tool for obtaining maximally-localised Wannier functions. *Comput. Phys. Commun.* **178**, 685-699 (2008).

54 Kuneš, J. *et al.* Wien2wannier: From linearized augmented plane waves to maximally

417 localized Wannier functions. *Comput. Phys. Commun.* **181**, 1888-1895 (2010).
418
419

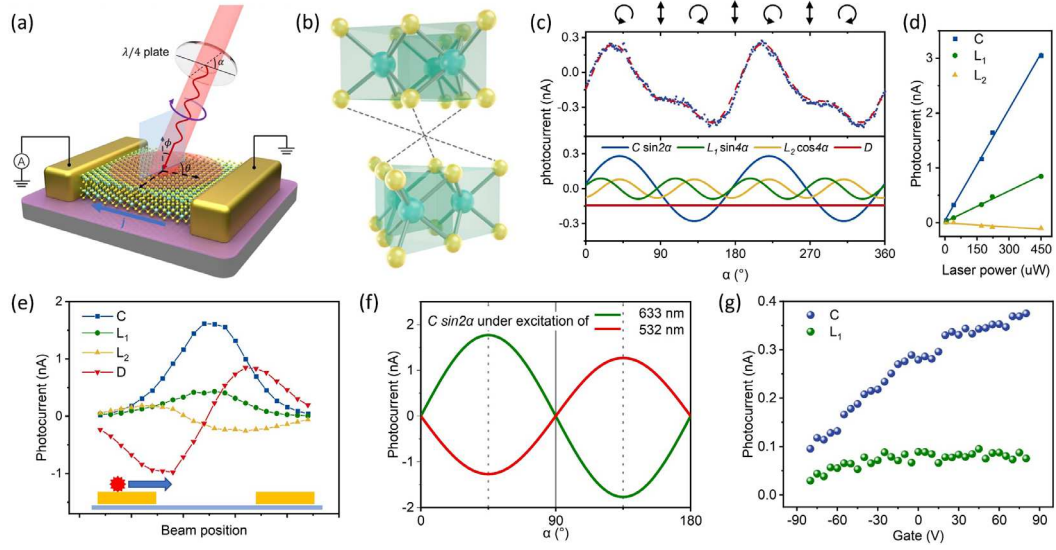


Figure 1. Observation of DC-related SONE in bilayer MoS₂. (a) Schematic diagram for the measurement of DC-related SONE with an incidence (azimuthal) angle Φ (θ). (b) Illustration of the crystal structure of bilayer MoS₂, the cross point of dot lines marks the center of spatial inversion symmetry. (c) Helicity-dependent photocurrent in bilayer MoS₂ as a function of the quarter-wave plate angle (upper panel). Blue (red) dot lines represent the measured (fitted) results. Lower panel: $C \sin 2\alpha$ (blue), $L_1 \sin 4\alpha$ (green) and $L_2 \cos 4\alpha$ extracted by fitting. (d) Power dependence of the DC-related SONE. (e) Position dependent DC-related SONE. (f) Helicity-resolved photocurrent versus radiation energy, under the excitations of 633 nm and 532 nm. (g) CPGE/LPGE as a function of back gate voltages.

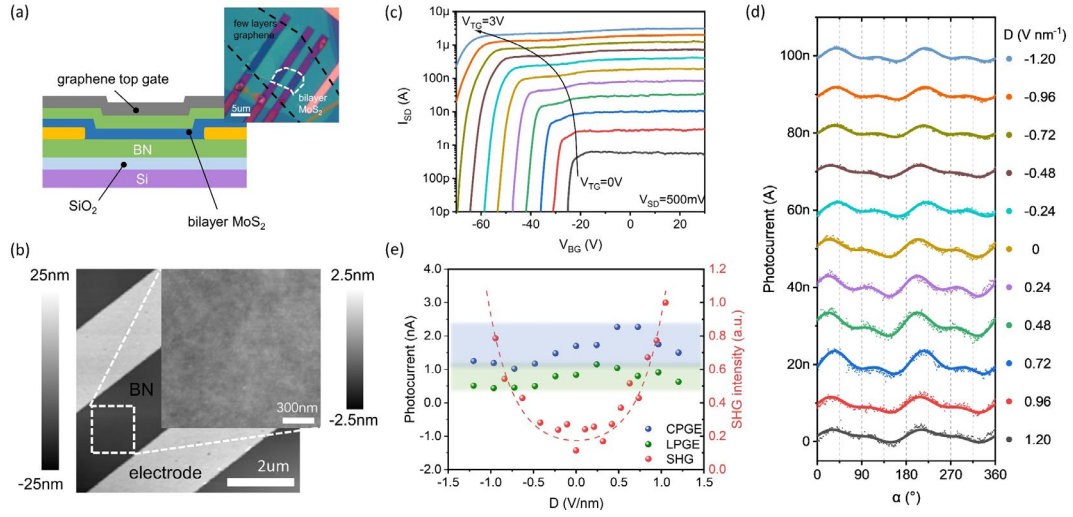


Figure 2. *D*-dependent SONE. (a) Schematic structure for a dual-gate bilayer MoS₂ device. Inset: Optical image of the dual-gate device. (b) The corresponding AFM image of (a). The zoom-in image shows the ultraclean interface. (c) Back gate transfer characteristics with different V_{TG} . (d) Polarization-dependent photocurrents detected under different D . (e) CPGE (blue dots) and LPGE (green dots) extracted from the photocurrents shown in (d), red dots are the detected SHG.

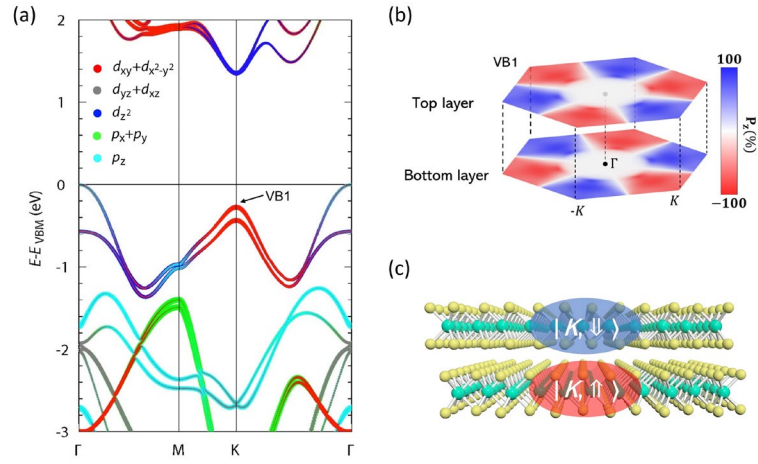


Figure 3. Valley dependent spin-layer locking in bilayer MoS₂. (a) Orbital projected band structure for bilayer MoS₂. Symbol size is proportional to its population in corresponding state. (b) Colour map of the out-of-plane spin polarization for the first valence band (VB1). (c) Illustrations of the spin-layer locking in bilayer MoS₂.

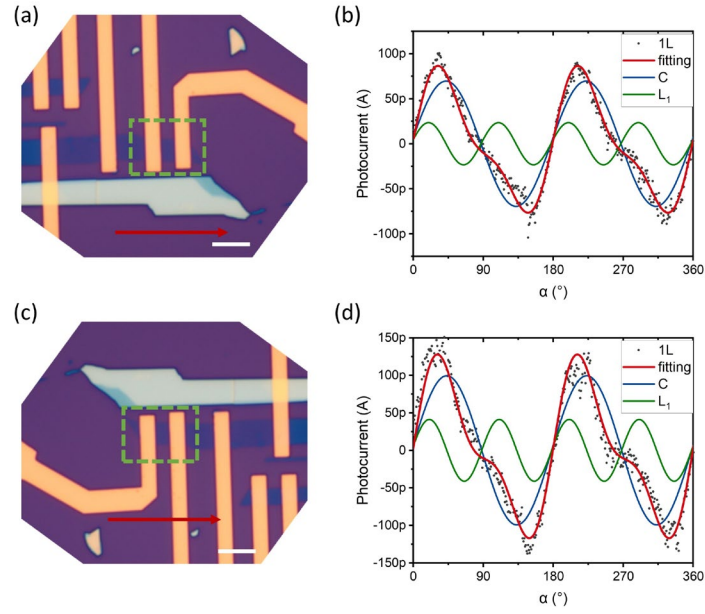


Figure 4. Rotation symmetry analysis of DC-related SONE. (a,c) Optical image of monolayer (green square) MoS₂ devices on SiO₂ before (a) and after (c) we rotate the device 180°. Scale bar, 5 μ m. (b) The helicity-dependent photocurrent and its fitting corresponding to configuration of (a). (d) Polarization-resolved photocurrent and its fitting corresponding to configuration of (c). The red arrow indicates the direction of photocurrent flow, and the photo-thermal current background D has been deducted for clarity.

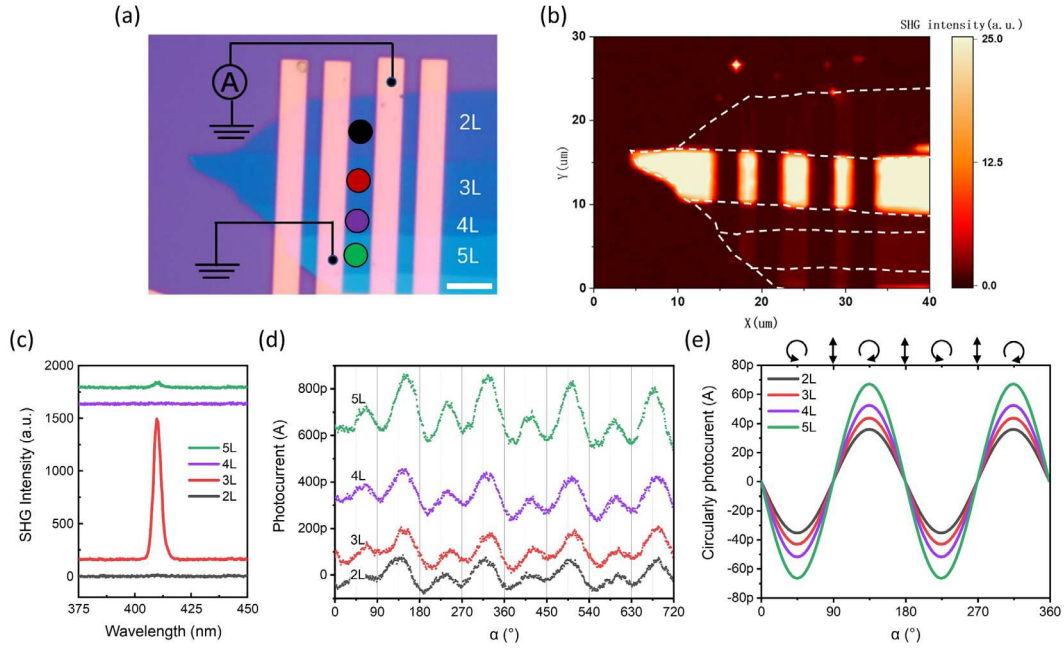


Figure 5. Layer-dependent DC-related SONE. (a) Optical image of MoS₂ field effect transistor devices with different channel thicknesses. Scale bar, 5 μm. (b) The corresponding SHG mapping of (a). (c) The SHG intensity versus the number of layers. (d) Polarization-resolved photocurrents with the laser located at the black, red, purple and green dots in (a). (e) Layer-dependent CPGE photocurrents extracted by fitting.

Figures

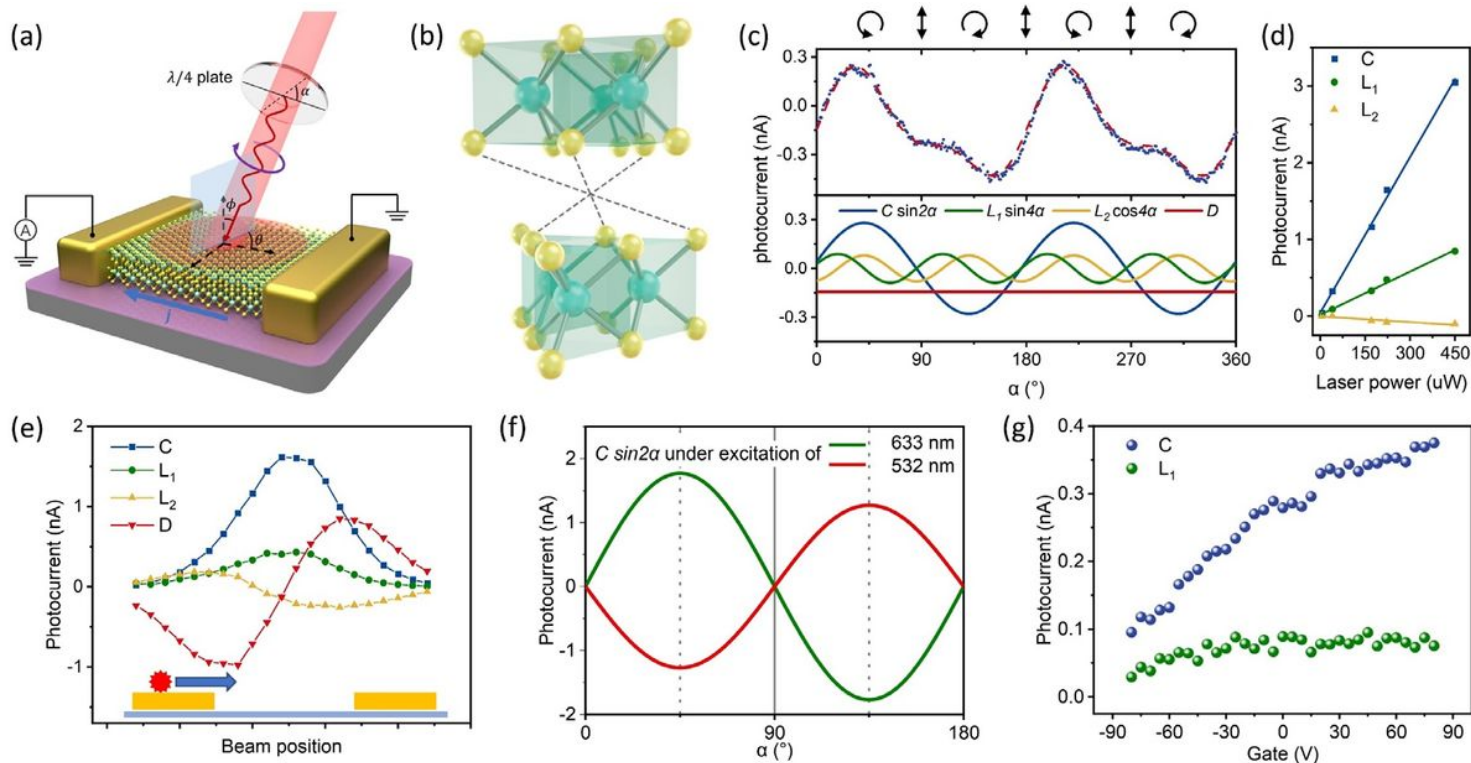


Figure 1

Observation of DC-related SONE in bilayer MoS₂. (a) Schematic diagram for the measurement of DC-related SONE with an incidence (azimuthal) angle Φ (θ). (b) Illustration of the crystal structure of bilayer MoS₂, the cross point of dot lines marks the center of spatial inversion symmetry. (c) Helicity-dependent photocurrent in bilayer MoS₂ as a function of the quarter-wave plate angle (upper panel). Blue (red) dot lines represent the measured (fitted) results. Lower panel: $C \sin 2\alpha$ (blue), $L_1 \sin 4\alpha$ (green) and $L_2 \cos 4\alpha$ extracted by fitting. (d) Power dependence of the DC-related SONE. (e) Position dependent DC-related SONE. (f) Helicity-resolved photocurrent versus radiation energy, under the excitations of 633 nm and 532 nm. (g) CPGE/LPGE as a function of back gate voltages.

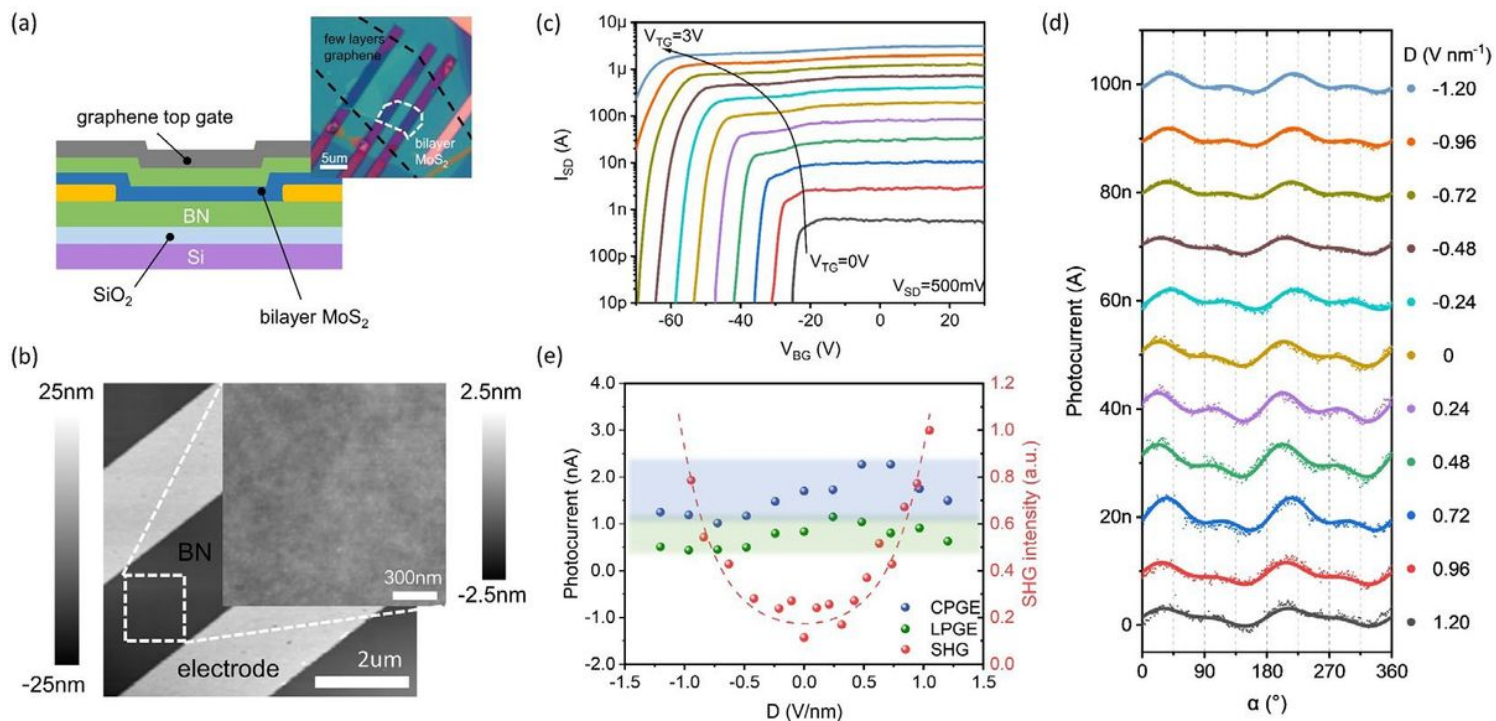


Figure 2

D-dependent SONE. (a) Schematic structure for a dual-gate bilayer MoS₂ device. Inset: Optical image of the dual-gate device. (b) The corresponding AFM image of (a). The zoom-in image shows the ultraclean interface. (c) Back gate transfer characteristics with different VTG. (d) Polarization-dependent photocurrents detected under different D . (e) CPGE (blue dots) and LPGE (green dots) extracted from the photocurrents shown in (d), red dots are the detected SHG.

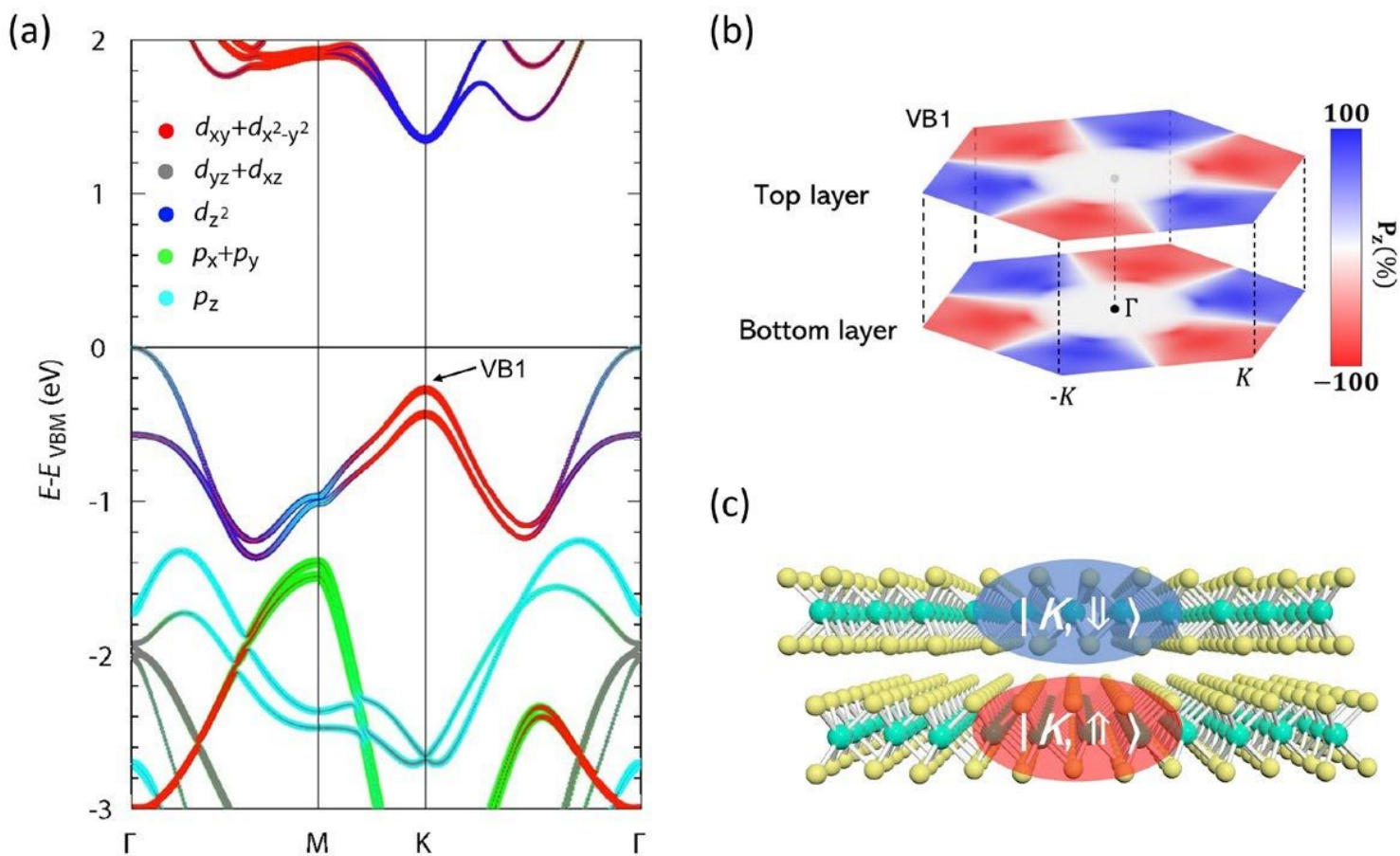


Figure 3

Valley dependent spin-layer locking in bilayer MoS₂. (a) Orbital projected band structure for bilayer MoS₂. Symbol size is proportional to its population in corresponding state. (b) Colour map of the out-of-plane spin polarization for the first valence band (VB1). (c) Illustrations of the spin-layer locking in bilayer MoS₂.

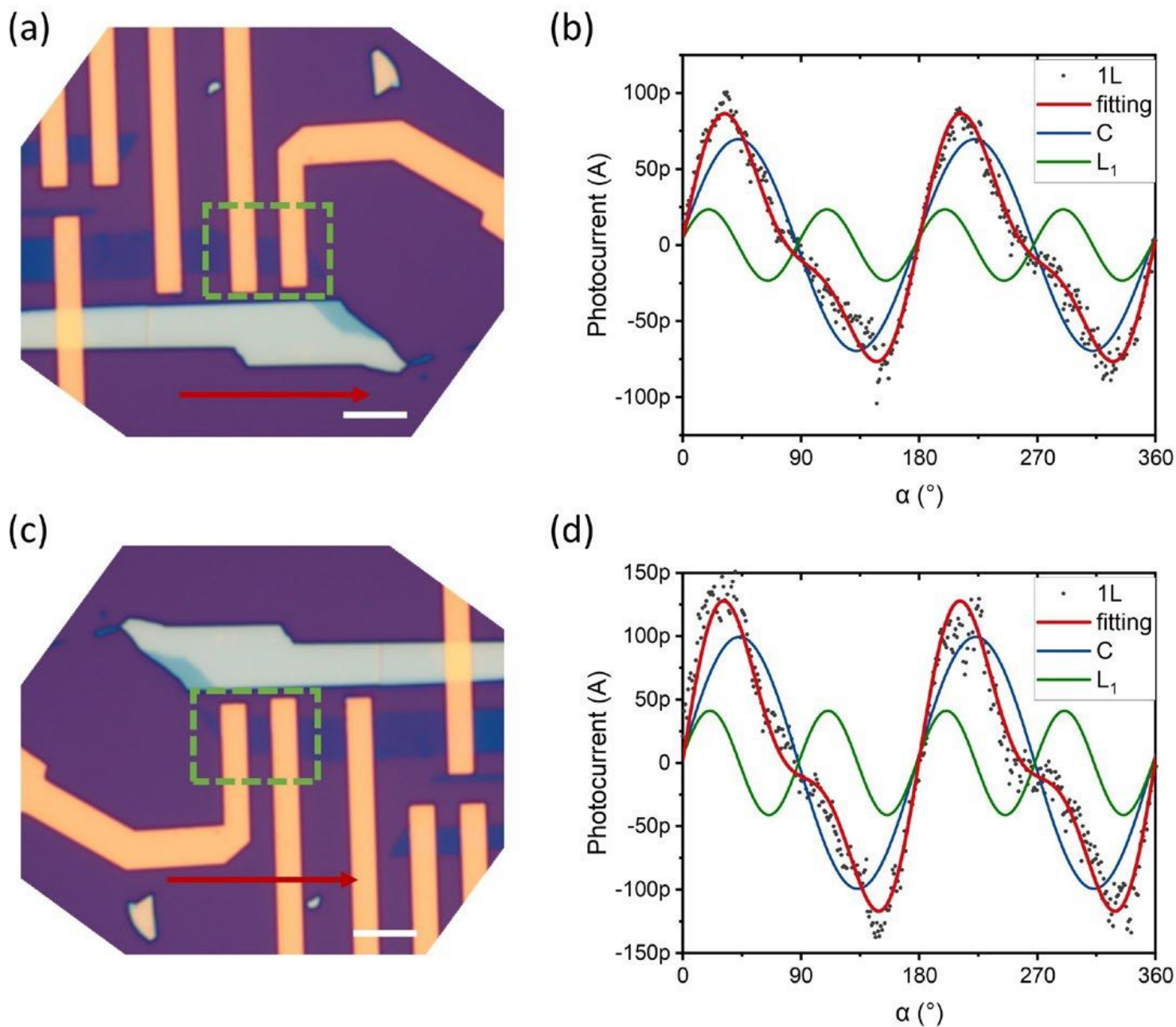


Figure 4

Rotation symmetry analysis of DC-related SONE. (a,c) Optical image of monolayer (green square) MoS2 devices on SiO2 before (a) and after (c) we rotate the device 180°. Scale bar, 5 μm . (b) The helicity-dependent photocurrent and its fitting corresponding to configuration of (a). (d) Polarization-resolved photocurrent and its fitting corresponding to configuration of (c). The red arrow indicates the direction of photocurrent flow, and the photo-thermal current background D has been deducted for clarity.

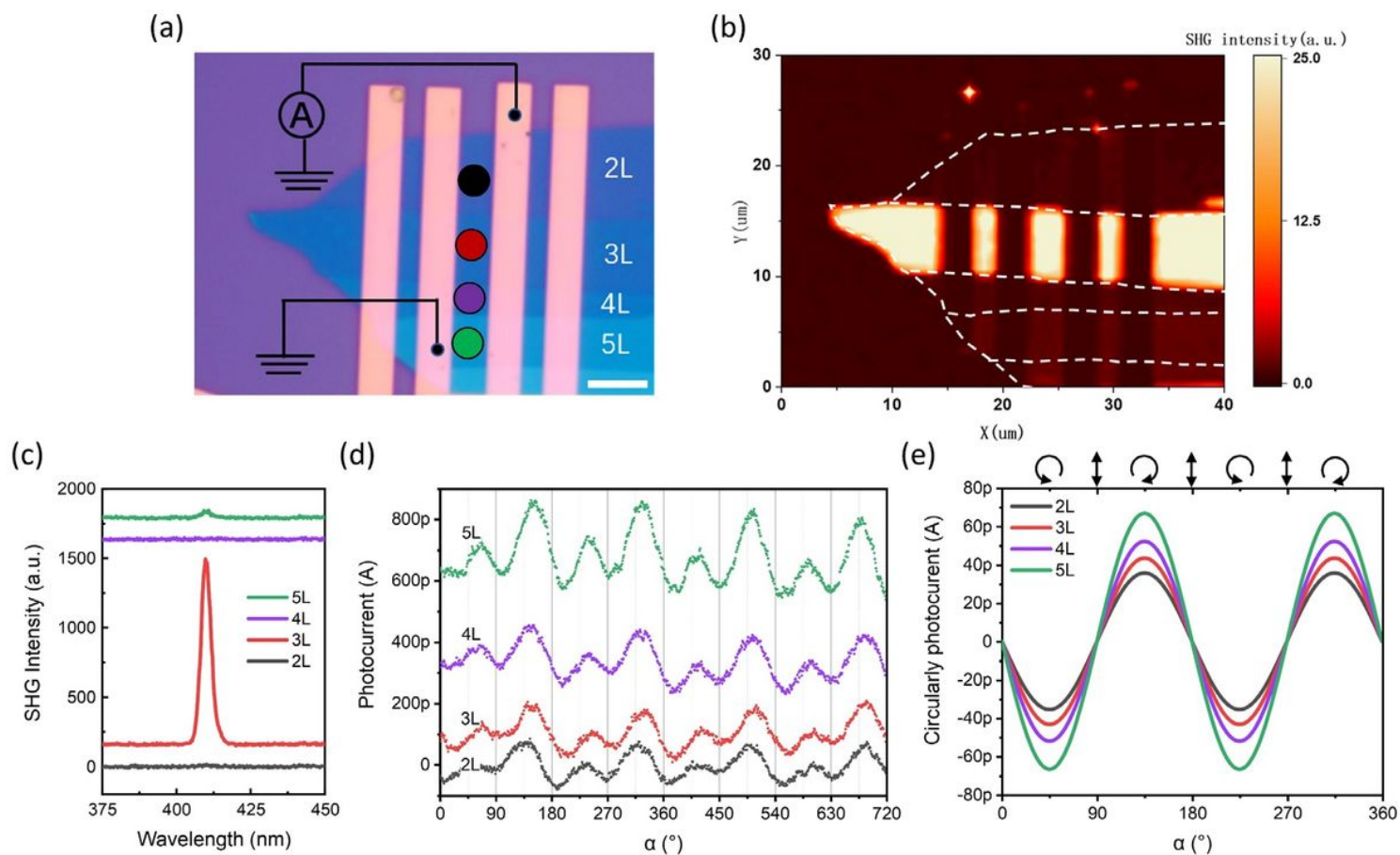


Figure 5

Layer-dependent DC-related SONE. (a) Optical image of MoS₂ field effect transistor devices with different channel thicknesses. Scale bar, 5 μm . (b) The corresponding SHG mapping of (a). (c) The SHG intensity versus the number of layers. (d) Polarization-resolved photocurrents with the laser located at the black, red, purple and green dots in (a). (e) Layer-dependent CPGE photocurrents extracted by fitting.

Supplementary Files

This is a list of supplementary files associated with this preprint. Click to download.

- [SupplementalMaterial.pdf](#)